AGU PUBLICATIONS

Journal of Advances in Modeling Earth Systems

RESEARCH ARTICLE
10.1002/2014MS000343

Investigating ice nucleation in cirrus clouds with an aerosol-enabled Multiscale Modeling Framework

Chengzhu Zhang[1], Minghuai Wang[2,3], Hugh Morrison[4], Richard C. J. Somerville[1], Kai Zhang[2], Xiaohong Liu[5], and Jui-Lin F. Li[6]

[1]Scripps Institution of Oceanography, University of California, San Diego, La Jolla, California, USA, [2]Pacific Northwest National Laboratory, Richland, Washington, USA, [3]Now at Professor at School of Atmospheric Sciences, Nanjing University, Nanjing, China, [4]National Center for Atmospheric Research, Boulder, Colorado, USA, [5]Department of Atmospheric Science, University of Wyoming, Laramie, Wyoming, USA, [6]Jet Propulsion Laboratory, California Institute of Technology, Pasadena, California, USA

Key Points:
- Aerosol-dependent ice nucleation is enabled in PNNL MMF
- New MMF captures persistent ice supersaturation and low ice number in cirrus
- MMF is powerful in emulating cloud processes evolving over short time scale

Correspondence to:
C. Zhang,
c5zhang@ucsd.edu

Citation:
Zhang, C., M. Wang, H. Morrison, R. C. J. Somerville, K. Zhang, X. Liu, and J.-L. F. Li (2014), Investigating ice nucleation in cirrus clouds with an aerosol-enabled Multiscale Modeling Framework, *J. Adv. Model. Earth Syst.*, *6*, 998–1015, doi:10.1002/2014MS000343.

Received 7 MAY 2014
Accepted 4 SEP 2014
Accepted article online 10 SEP 2014
Published online 6 NOV 2014

Abstract In this study, an aerosol-dependent ice nucleation scheme has been implemented in an aerosol-enabled Multiscale Modeling Framework (PNNL MMF) to study ice formation in upper troposphere cirrus clouds through both homogeneous and heterogeneous nucleation. The MMF model represents cloud scale processes by embedding a cloud-resolving model (CRM) within each vertical column of a GCM grid. By explicitly linking ice nucleation to aerosol number concentration, CRM-scale temperature, relative humidity and vertical velocity, the new MMF model simulates the persistent high ice supersaturation and low ice number concentration (10–100/L) at cirrus temperatures. The new model simulates the observed shift of the ice supersaturation PDF toward higher values at low temperatures following the homogeneous nucleation threshold. The MMF model predicts a higher frequency of midlatitude supersaturation in the Southern Hemisphere and winter hemisphere, which is consistent with previous satellite and in situ observations. It is shown that compared to a conventional GCM, the MMF is a more powerful model to simulate parameters that evolve over short time scales such as supersaturation. Sensitivity tests suggest that the simulated global distribution of ice clouds is sensitive to the ice nucleation scheme and the distribution of sulfate and dust aerosols. Simulations are also performed to test empirical parameters related to auto-conversion of ice crystals to snow. Results show that with a value of 250 μm for the critical diameter, Dcs, that distinguishes ice crystals from snow, the model can produce good agreement with the satellite-retrieved products in terms of cloud ice water path and ice water content, while the total ice water is not sensitive to the specification of Dcs value.

1. Introduction

Cirrus clouds have important effects on Earth's radiation budget because of their large global coverage (about 30%) and their high formation altitude [*Lynch*, 2002]. They have opposing radiative effects by reflecting solar radiation back to space (cooling) and trapping infrared radiation similarly to greenhouse gases (warming). These radiative effects depend on the cloud macrophysical properties (thickness, altitude, temperature) as well as the microphysical properties of the ice crystals these clouds contain. Therefore, microphysical processes such as ice nucleation, ice diffusional vapor growth and aggregation are critical in determining the net radiative forcing of cirrus clouds [*Lynch*, 2002; *DeMott et al*., 2010]. In addition, the mechanism of ice nucleation on aerosols and the distribution of ice in clouds can influence global precipitation, which in turn affects the surface energy balance and the hydrologic cycle [*Waliser et al*., 2009].

The formation mechanisms of ice particles in the atmosphere, however, remain poorly understood [IPCC AR5, 2013]. The difficulty in studying ice cloud formation stems from complicated ice initiation pathways: ice particles can form either by homogenous freezing of solution droplets or by heterogeneous freezing on ice nuclei (IN). The latter process has been further subdivided in the literature into four modes: immersion, deposition, contact and condensation freezing [*Pruppacher and Klett*, 1997]. Though homogeneous freezing of solution droplets has been quantitatively constrained [*Koop et al*., 2000], it remains challenging to identify the activity of various materials as IN, due to multiple nucleation modes. The effectiveness of those materials serving as IN in heterogeneous nucleation remains an open issue [*Cantrell and Heymsfield*, 2005; *Murray et al*., 2012; *Hoose and Möhler*, 2012]. By analyzing the residual particle composites collected within cirrus,

Cziczo et al. [2013] recently pointed out that dust and metallic particles are dominant IN under upper tropospheric conditions. They also suggested that heterogeneous nucleation dominated homogeneous freezing, contributing to 94% of cloud encounters at cirrus temperatures. During recent years, emerging observations of upper tropospheric humidity and ice number concentration based on in situ and satellite measurements [i.e., *Gettelman et al*., 2006; *Lawson et al*., 2008; *Krämer et al*., 2009] indicate that the occurrence of heterogeneous nucleation is probably the most obvious reason to explain observed prevailing ice supersaturation, low ice concentration and broad ice crystal size distributions [*Jensen et al*., 2010].

Despite the relatively low level of understanding of heterogeneous nucleation, a few physically based parameterizations that treat the competition between homogeneous and heterogeneous nucleation have been developed for general circulation models (GCMs) in order to study the global effect of ice nucleation [*Kärcher et al*., 2006; *Liu and Penner*, 2005; *Barahona and Nenes*, 2009]. Global numerical simulation experiments of aerosol effects on ice cloud formation have been carried out with a number of GCMs, i.e., European Centre/Hamburg (ECHAM) model [*Kärcher and Lohmann*, 2002; *Lohmann et al*., 2008], and NCAR Community Atmosphere Model (CAM) [*Liu et al*., 2007; *Penner et al*., 2009; *Wang and Penner*, 2010; *Gettelman et al*., 2010; *Liu et al*., 2012a]. It has been shown that conventional GCMs have substantial difficulty in simulating the evolution of cirrus clouds, because many of the dynamic processes that drive cirrus cloud formation are not explicitly resolved with the relatively coarse spatial and temporal model resolutions of these GCMs [*Liu et al*., 2007; *Gettelman et al*., 2010]. For example, in cirrus formation processes, once ice particles form, they deplete the surrounding water vapor until the supersaturation relaxes to an equilibrium static state (under constant dynamical forcing). The time scale of water vapor relaxation ranges from seconds to as long as hours depending on temperature, updraft velocity, nucleation mechanisms, and other factors [*Khvorostyanov et al*., 2006; *Kärcher and Burkhardt*, 2008]. Most current GCMs have difficulty in realistically representing the variability of these quantities, which are critical to the ice nucleation rate, because of the relatively long model time step and coarse grid spacing [*Wang and Penner*, 2010; *Hendricks et al*., 2011]. Therefore, traditional GCMs tend to neglect some microphysical effects, such as the impact of preexisting ice on new ice formation. The deposition of water vapor onto preexisting cloud ice particles could inhibit the nucleation due to suppressed supersaturation, in turn modify ice particle formation [*Kärcher et al*., 2006]. Thus, special treatment is required to represent this preexisting ice effect in these GCMs [*Hendricks et al*., 2011; *Kuebbeler et al*., 2013].

In this paper, we present a global study of ice nucleation with the aerosol-enabled Pacific Northwest National Laboratory Multiscale Modeling Framework (PNNL MMF). The Multiscale Modeling Framework (MMF) is an approach to global modeling that embeds a cloud-resolving model (CRM) within each grid column of a traditional GCM to replace conventional cloud parameterizations (also known as superparameterization) [*Khairoutdinov and Randall*, 2001]. In this type of model, cloud system scale (10 km) as well as large-scale (100–200 km) circulations are resolved within a single framework. The MMF has been shown to improve many aspects of convective variability including the intraseasonal variability associated with the Madden-Julian oscillation (MJO) and the diurnal cycle of precipitation over the continents [*Khairoutdinov et al*., 2008; *Tao et al*., 2009; *Pritchard et al*., 2011; *Kooperman et al*., 2013].

In the MMF, the representation of the cloud microphysical processes can have a large impact on climate simulations, not only because of the coupling of microphysics and radiation as in traditional GCMs, but also because cloud microphysics in the MMF is directly coupled with convection. The newest version of the MMF, developed at PNNL [*Wang et al*., 2011b], now updates the host GCM to the Community Atmosphere Model version 5 (CAM5) and includes aerosol interactions with a two-moment cloud microphysics scheme. This model is an extension of the Colorado State University (CSU) MMF originally implemented in the National Center for Atmospheric Research (NCAR) Community Atmosphere Model version 3 (CAM3) by *Khairoutdinov and Randall* [2001].

Previous results from CSU MMF indicated that the model overpredicts cloud cover in the tropical western Pacific, the Indian Ocean and along the equatorial central and eastern Pacific. This defect is largely due to an overprediction of high clouds due to overactive convection and the model microphysical treatment of ice cloud formation in these tropical regions [*Zhang et al*., 2008; *Marchand and Ackerman*, 2010]. Ice nucleation processes in the CSU MMF are not explicitly treated using a one-moment microphysics scheme, while in the original PNNL MMF, ice nucleation is temperature-dependent only [*Cooper*, 1986] and is therefore unable to simulate aerosol effects on cirrus clouds. In the present study, we have implemented an aerosol-

dependent ice nucleation scheme in the PNNL MMF and have evaluated the role of ice nucleation in cirrus formation. We present a detailed model description and experiment design in Section 2, the model evaluation and analysis of global ice nucleation in Section 3, and a discussion and summary in Section 4.

2. Model Description and Experiment Design

2.1. Aerosol-Enabled MMF (PNNL-MMF)

The concept of representing clouds in a MMF was originally introduced by *Grabowski* [2001]. *Khairoutdinov and Randall* [2001] further developed this approach and first embedded a two-dimensional version of a cloud resolving model (System for Atmospheric Modeling, SAM) within a realistic GCM: CAM3. In the PNNL MMF, the host GCM was updated to version 5 (CAM5), and a two-moment microphysics scheme [*Morrison et al*., 2005, 2009] is employed in place of the one-moment scheme used in the CSU MMF. Moreover, an Explicit-Cloud Parameterized-Pollutant (ECPP) approach [*Gustafson et al*., 2008] is used to couple cloud simulations in the CRM with the modal representation of aerosol (Modal Aerosol Module, MAM)[*Liu et al*., 2012b] in CAM5, which makes it possible for the MMF to be used for the study of cloud-aerosol interactions from cloud scales to global scales.

The cloud-resolving model embedded in each GCM grid column solves the nonhydrostatic momentum equations. Moisture, thermodynamic, and momentum tendencies from the host global model drive the CRM, and the CRM feeds back vertical fluxes of heat and moisture to the host model. This model structure implies that, unlike the separate convective and stratiform parameterizations employed in traditional GCMs, cloud processes in the MMF, including microphysics and cloud-aerosol interactions, are explicitly treated for all types of cloud. Model details can be found in *Wang et al*. [2011b] and references therein. Despite the fundamentally different methods of representing clouds in MMFs versus conventional GCMs, the dynamical core is the same for PNNL-MMF and CAM5, because PNNL-MMF employs CAM5 as its host GCM component.

2.2. Ice Nucleation Schemes

Results from simulations with the PNNL-MMF (hereafter MMF) have indicated that the predicted aerosol radiative forcing is in better agreement with observations and high-resolution models than that calculated from a GCM with conventional cloud parameterizations [*Wang et al*., 2011a, 2012; *Kooperman et al*., 2012]. *Wang et al*. [2011a] documented a radiative cooling of -0.77 Wm^{-2} from changes in the shortwave cloud forcing (shortwave aerosol indirect effect) due to anthropogenic aerosols. The cooling is significantly smaller than that simulated by CAM5, because the liquid water path in MMF is less sensitive to the change of aerosol loading. However, as ice nucleation is not directly linked to aerosol particles in the study of *Wang et al*. [2011a], the estimate of the aerosol indirect effect does not include aerosol effects on ice clouds. This important shortcoming points to the need to improve the treatment of ice nucleation in the MMF.

The original ice formation in the CRM in the MMF follows the formulations in the two-moment microphysics scheme of *Morrison et al*. [2005, 2009]. Ice is nucleated following *Cooper* [1986] formulation, when conditions are either saturated with respect to liquid water and with a temperature less than -8°C, or when relative humidity over ice is greater than 108%. The nucleated ice number is a simple function of temperature and is limited to a maximum of 500 L^{-1} at each time step to eliminate unreasonably large numbers of ice particles. Homogeneous freezing of haze aerosols and heterogeneous freezing on the introduction of ice nuclei (IN) are not explicitly considered in this version of the scheme. In this study, we implement an ice crystal nucleation scheme based on that of *Liu and Penner* [2005] (hereafter LP05) in the CRM component of the MMF.

In the LP05 scheme, the number of nucleated ice crystals, Ni, is derived by fitting Ni to cloud parcel model experiment results. Ni is a function of temperature, humidity, updraft velocity and aerosol number concentrations. Following CAM5 [*Gettelman et al*., 2010; *Neale et al*., 2010], only sulfate and dust are considered to nucleate ice. In the MAM aerosol treatment [*Liu et al*., 2012b], aerosols are grouped into three (MAM3) or seven (MAM7) modes. We employ MAM3, in which major aerosol species are grouped into Aitken, accumulation and coarse modes. MAM then predicts the mass mixing ratio of different aerosol species in each mode and the number mixing ratio of each mode. In previous relevant studies employing CAM5, the sulfate and dust aerosols that can nucleate ice are selected differently from within the modes. *Gettelman et al*.

[2010] used a portion of the Aitken mode sulfate with diameter greater than 100 nm and only coarse mode dust in the ice nucleation, in order to limit modeled ice number concentration to be consistent with observations. In contrast, *Liu et al*. [2012a] used all the Aitken mode sulfate and both accumulation and coarse mode dust.

For pure ice clouds with $T < -37°C$, the LP05 scheme features homogeneous nucleation on sulfate aerosols and heterogeneous immersion nucleation on mineral dust. The threshold relative humidity for homogeneous ice formation depends on temperature and vertical velocity on the CRM grid, for which temperature is the dominant control [*Liu and Penner*, 2005]. Ice crystal number density from homogeneous nucleation is formulated in two sets of formulas for two growth regions: higher temperature and lower vertical velocity (the fast-growth regime) and lower temperature and higher vertical velocity (the slow-growth regime). At the slow-growth regime homogeneous nucleation shows a strong dependence on sulfate particle number. The threshold relative humidity with respect to ice (RHi) for heterogeneous immersion freezing is 120%, which is around 30% to 40% smaller than RHi calculated for homogeneous freezing. For heterogeneous immersion nucleation on dust, classical nucleation theory (CNT) was the basis for the ice nucleation parameterization developed via parcel model simulations. In CNT, the ice nucleation treatment assumes a single parameter (contact angle) to describe the ice nucleation efficiency of dust particles to freeze purely stochastically. Similar to *Gierens* [2003], the competition between both freezing pathways in LP05 is controlled primarily by the critical IN number concentration which is a function of temperature and vertical velocity: when IN is higher than this critical number, homogeneous nucleation is suppressed and only heterogeneous nucleation occurs. The ice crystal numbers formed from the two nucleation mechanisms are then calculated from the given temperature, vertical velocity and sulfate number concentration or dust number concentration, respectively (LP05) [*Liu et al*., 2007]. We note here that the LP scheme implemented in our model is an important factor for this study, not necessarily its full representativeness of ice nucleation in detail. For instance, there are still large uncertainties with vertical velocity and IN number from observations and in the treatment of these two variables in large-scale models. This aim of this study is to provide a framework to explore the sensitivity of dominant ice nucleation mechanism to these variables on the global scale. Future in situ observations can help to quantify the properties of aerosols that enable ice nucleation and to identify the nucleation mechanisms.

For mixed phase clouds ($-37\ °C < T < 0\ °C$), ice nucleation on aerosol is kept the same as in the original PNNL-MMF, following Cooper [1986]. Freezing of cloud water and rain remains the same as in *Morrison et al*. [2005, 2009]. Although several more recent mixed phase cloud ice nucleation schemes have been developed that explicitly link to aerosols [e.g., *Phillips et al*., 2008; *DeMott et al*., 2010; *Hoose et al*., 2010; *Wang et al*., 2014], by keeping the original scheme we are able to focus on cirrus clouds and avoid complications due to changes in the treatment of nucleation in mixed-phase clouds. Future work on mixed phase clouds will be conducted.

Since the embedded CRM cannot resolve radiatively driven turbulence that is likely to be important for cirrus, following the approach to calculate vertical velocity to drive droplet activation in the MMF [*Wang et al*., 2011b], we calculate the vertical velocity used in ice nucleation as a sum of the resolved velocity at the CRM grid and a subgrid vertical velocity that represents the unresolved motion. The CRM subgrid vertical velocity is diagnosed from the turbulent kinetic energy, which is further diagnosed from the eddy viscosity. We set a minimum value of 0.2 m/s for the CRM subgrid vertical velocity. We note here that from CAM5.0 onward, an upper bound of 0.2 m/s is enforced for subgrid updraft velocity for ice nucleation, in order to avoid unrealistically high ice number concentration. By including the effect of preexisting ice particles, *Shi et al*., [2014] are able to remove the upper limit of 0.2 m/s used in CAM5. Nevertheless, the calculation of updrafts in MMF is fundamentally different from that in CAM5, and the effects of updraft velocity on the ice nucleation in cirrus clouds remain to be investigated with MMF in a future study.

2.3. Experiment Design

The simulation setup and aerosol emission follows that of *Wang et al*. [2011a]: The host GCM CAM5 uses the finite-volume dynamical core at $4° \times 5°$ horizontal grid resolution and a time step of 10 min. The model uses climatological sea surface temperatures (SSTs) and sea ice. The embedded CRM has a horizontal grid spacing of 4 km, with 28 vertical levels colocated with CAM's lowest 28 levels (the host CAM has 30 vertical levels), and the CRM is run in two dimensions with a north-south orientation. The CRM is run in a nested

Table 1. Simulation Cases in This Study

Simulation	Description
MMF0	Cooper [1986], Dcs=125 μm
LP	LP 2005, default CAM5 aerosol, Dcs=125 μm
LPHI	LP, higher portion of aerosol for nucleation, Dcs=125 μm
LP250	LP, Dcs=250 μm
LPHI250	LPHI, Dcs=250 μm
CAM5	LP 2005, default CAM5 aerosol, Dcs=300 μm

integration with a time step of 20 s, which is 30 times shorter than the outer host GCM time step (10 min). Each CRM is run independently within each GCM grid column using periodic lateral boundary conditions. Anthropogenic aerosol and precursor gas emissions are from the *Lamarque et al*. [2010] IPCC AR5 emission data set. This study uses year 2000 emissions.

Five sets of MMF simulation are carried out (Table 1): one for the original MMF with the Cooper 1986 ice nucleation scheme and four sets of simulations with the LP05 scheme: LP, LP250, LPHI and LPHI250. The LP cases (LP and LP250) use the default sulfate and dust aerosol setting for ice nucleation as in the standard CAM5 [*Gettelman et al*., 2010], in which a lower size limit is set for sulfate and dust aerosols that can possibly activate in ice nucleation. By contrast, the LPHI cases (LPHI and LPHI250, where HI indicates higher portion from aerosol modes as inputs to ice nucleation) apply all Aitken mode sulfate and both coarse and accumulation mode dust as candidate aerosols for ice nucleation. The latter setting follows the study by *Liu et al*. [2012a], which suggested that smaller particles could be involved in the initiation of ice nucleation. *Shi et al*. [2014] also suggested that the size constraint for Aitken mode sulfate could be removed if the preexisting ice effect is specially treated in CAM5. In our case, simulations of both scenarios have been carried out to test the model sensitivity. In the third variation of LP simulations (LP250 and LPHI250), we increase the ice-to-snow auto-conversion size threshold (critical crystal diameter, Dcs) from 125 to 250 μm. *Zhang et al*. [2013] suggested that ice water path and thus longwave cloud forcing in CAM5 are sensitive to the value of Dcs and that a value 250 μm successfully reproduces ice number concentration and effective radius obtained from the SPARTICUS campaign. Lastly, a $1.9^\circ \times 2.5^\circ$ resolution CAM5 simulation with default aerosol setting is carried out for comparison.

In total, 27 months simulation period is run for each configuration (listed in Table 1), and the last 24 months of results are used for analysis.

3. Results and Model Evaluation

In this section, we evaluate the model from a global perspective and present model results on ice particle number, ice supersaturation and ice water content or path (IWC or IWP), and we compare these model results with available observations to study ice formation processes in cirrus cloud.

3.1. Distribution of Ice and Aerosol Particles

Figure 1 shows the annually averaged global distribution of column-integrated (top plot) and zonal mean (bottom plot) grid-averaged ice crystal number concentration simulated from MMF0, LP and LPHI. When only a portion of Aitken mode sulfate is taken into account for homogenous nucleation (LP case), ice production is reduced globally, with column-integrated ice crystal number concentration (0.45×10^8 m^{-2}) less than 1/4 of that from MMF0. The low ice number results in small IWP, and hence leads to underestimation of longwave cloud radiative forcing (see Table 2). The LPHI case produces a global mean ice number similar to that of MMF0 (1.82×10^8 m^{-2} versus 2.0×10^8 m^{-2}). In the LPHI case, higher ice concentration is predicted in the tropical upper troposphere and the Southern Hemisphere (SH) high latitudes than LP, corresponding to regions with higher number concentration of sulfate aerosols (Figure 2), while ice number concentrations in the SH middle latitudes (30°S to 50°S) are lower in LP and LPHI than in MMF0 due to low sulfate and dust concentrations over the SH ocean. In MMF0, the tropics have the highest ice number due to deep convection over the tropical western Pacific, the Indian Ocean and along the equatorial central and eastern Pacific.

The zonal distribution of sulfate and dust aerosols that can form ice differs substantially for the two aerosol settings (Figure 2). The number concentration of Aitken mode sulfate aerosols that is input into the ice nucleation in the LPHI case is 2–3 orders of magnitude higher than that used in the LP case, in the tropical upper troposphere. As expected, a majority of Aitken mode sulfate has a diameter smaller than 0.1 μm there. The concentration peaks in the tropical upper troposphere and the SH middle troposphere are

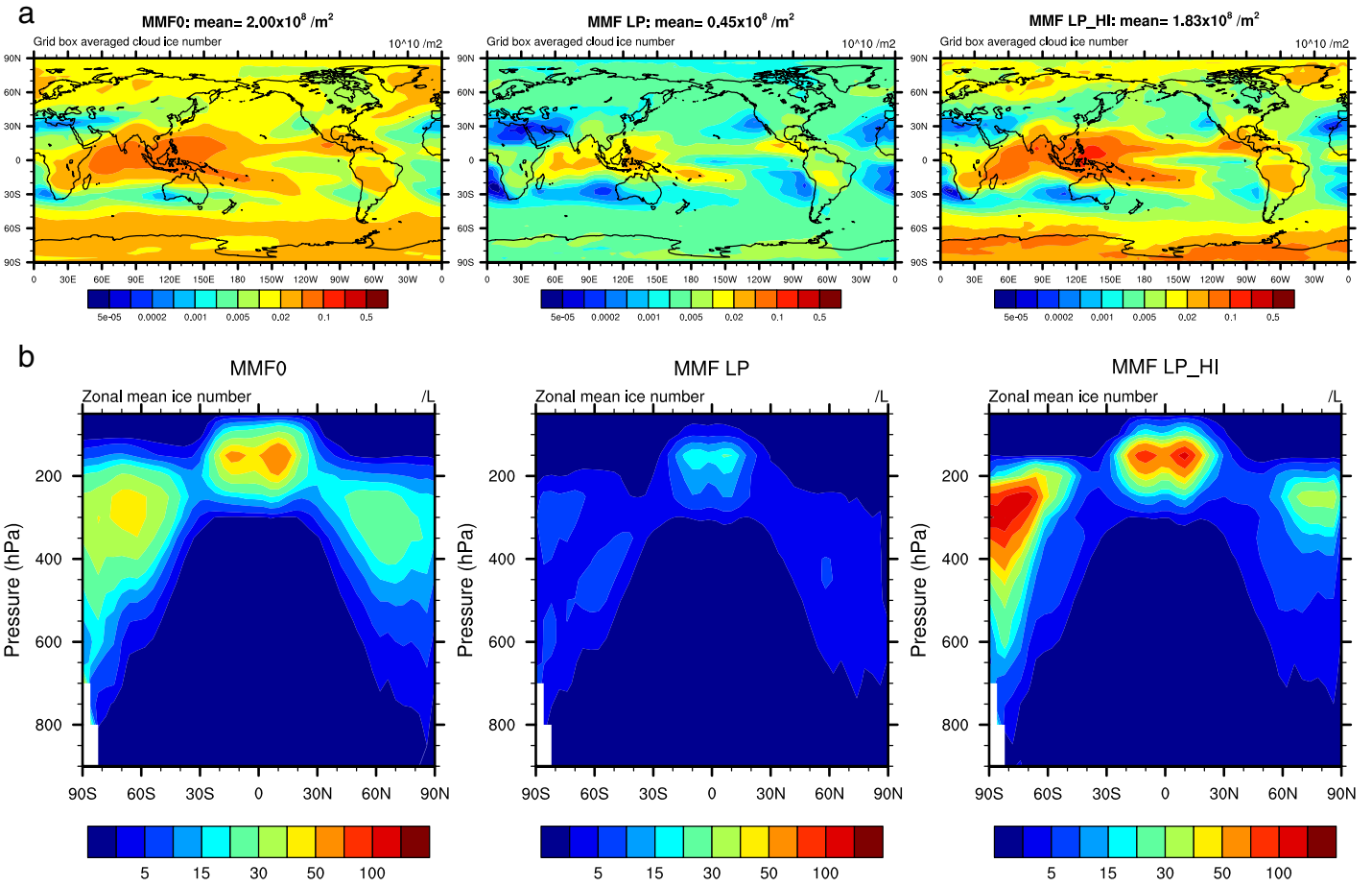

Figure 1. Annual mean global distribution of ice number concentration: (top) column-integrated ice number ($\times 10^{10}$ m^{-2}) and (bottom) zonal mean ice number (L^{-1}) simulated from three models: (left) MMF0, (middle) LP, and (right) LPHI.

caused by the binary homogeneous nucleation of H2SO4 and H2O, which is favored at low temperature, high relative humidity and small aerosol surface area [*Easter and Peters*, 1994]. The spatial distribution of mineral dust particles that act as heterogeneous IN is similar for both LP and LPHI cases. The major dust source is from Northern Hemisphere deserts. The maximum concentration is about one order of magnitude higher in LPHI than in LP.

3.2. Ice Number Concentration

Ice number concentration measurements from field programs are highly localized, and different programs employ different probes and measurement techniques. This heterogeneity in observations poses great difficulties for any attempt at directly comparing observations and data sets from global models. Atmospheric models also typically use artificial thresholds (e.g., Dcs) to separate ice phase hydrometer types, i.e., cloud ice and snow. Cloud ice is characterized by small pristine ice particles that have an assumed terminal velocity of zero. Snow consists of larger particles that have a nonzero terminal velocity and are able to precipitate [*Schmitt and Heymsfield*, 2014]. The value of Dcs therefore also determines the size of the particles that remain in the atmosphere, which in turn has impacts on the radiative properties of the ice clouds. In our case, cloud ice number concentration (Ni) refers to ice in the model cloud ice category and excludes snow; therefore Ni will not represent all ice particles. In this section, we use available observational data from several sources to evaluate statistics of the modeled ice number concentration.

Figure 3 shows the simulated in-cloud ice crystal number concentration range between the 25th and 75th percentiles versus temperature. The model data are from 150 to 300 mb height from 30°S and 60°N where in situ data are available. Simulated Ni from all three cases display a slight decreasing trend with increasing

Table 2. Global Annual Mean Cloud Properties From Sensitivity Simulations Listed in Table 1 for Shortwave Cloud Forcing (SWCF, Wm^{-2}), Longwave Cloud Forcing (LWCF, Wm^{-2}), Liquid Water Path (LWP, gm^{-2}), Ice Water Path (IWP, gm^{-2}), Total Cloud Cover (CTOT, %), High Cloud Cover (CHGH, %), and Column Ice Number Concentration (NUMI, $\times 10^8$ m^{-2})[a]

Cases	SWCF	LWCF	LWP	IWP	CTOT	CHGH	NUMI
MMF0	−50.5 (−50.5)	27.0 (26.0)	53.2 (55.9)	11.1 (9.91)	50.0 (55.8)	28.0 (29.2)	2.00 (2.12)
LP	−45.6	19.6	52.3	6.8	45.3	20.7	0.45
LPHI	−47.8	21.9	53.0	8.1	46.5	22.6	1.82
LP250	−46.7	22.2	54.0	24.4	52.0	26.2	0.65
LPHI250	−49.0	24.9	54.3	26.3	53.0	29.1	2.32
CAM5	−50.1	21.9	48.4	16.1	62.7	37.6	1.00
OBS	−46 to −53	27–31					

[a]The values in parentheses in MMF0 simulation are for results from 1.9°×2.5° simulation, cited from *Wang et al.* [2011b]. The observed SWCF and LWCF are from satellite products ERBE and CERES [*Loeb et al.*, 2009]. CAM5 simulation has 1.9° × 2.5° resolution.

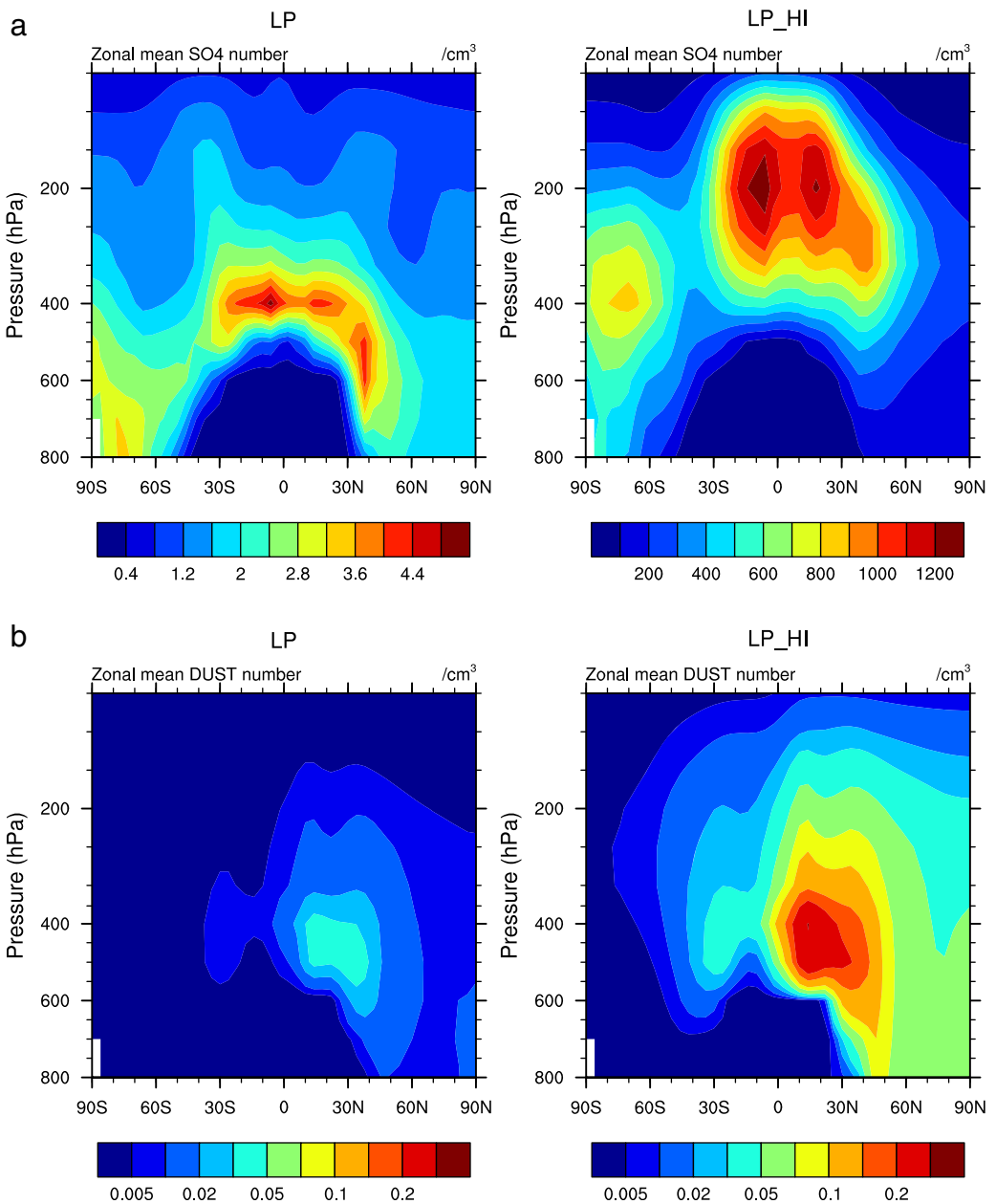

Figure 2. Annual mean zonal mean number concentration (cm^{-3}) of (top) sulfate aerosol and (bottom) mineral dust that can nucleate ice simulated from (left) LP and (right) LPHI. Note different color bars for sulfate number concentration.

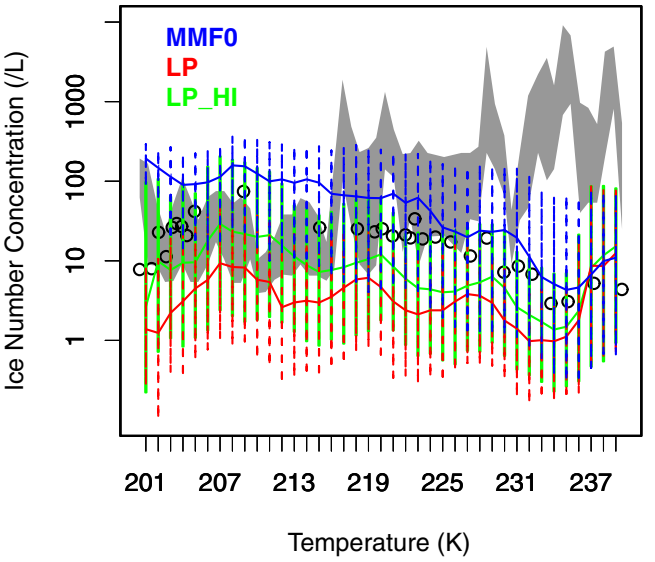

Figure 3. Model results of in-cloud ice crystal number concentration (L^{-1}) versus temperature, which are sampled every 3 h over regions from 30°S to 60°N from MMF0 (blue), LP (red) and LPHI (green). (We define grid points that have Ni > 0.01 L^{-1} as in cloud points.) The median value for each temperature bin (1 K) follows the curves, the 25th and 75th percentiles are indicated by the vertical dashed lines. The shaded areas are observation from the campaign sites reported by *Krämer et al*. [2009]. The black circles are reproduced from *Heymsfield et al*. [2013, Figure 4], indicating median values of ice number concentrations measurements collected from 10 field programs.

temperature. This trend is opposite to that was reported by *Krämer et al*., [2009] (gray shades in Figure 3). However, there is increasing evidence that the high Ni reported at higher temperatures is a measurement bias caused by large ice crystals shattering on the cloud probes [e.g., *McFarquhar et al*., 2007]. Moreover, during the recent SPARTICUS campaign, the observed Ni decreased with increasing temperature over the U. S. Southern Great Plains (SGP) [*Zhang et al*., 2013]. The study by *Heymsfield et al*. [2013] analyzed ice number concentration collected from ten field programs (black circles in Figure 3). In their study, a median value of 27/L is assigned to Ni for temperature colder than −60°C; for −60 to 0°C, Ni is fitted to an exponentially decreasing function.

In our simulations, at low temperatures (<210 K), the case MMF0 predicts a high frequency of large Ni ranging from 100 to 1000 per liter, which is about 10 times higher than observed [*Krämer et al*., 2009; *Liu et al*., 2012a; *Gettelman et al*., 2012], while LP under-predicts the ice number concentration by a factor of 10 and LPHI matches lower values in the observation range. When compared to data reproduced from *Heymsfield et al*. [2013], LPHI predicts a similar median number of Ni at around 200 K, while Ni is under-predicted for higher temperatures. At this temperature range, concentrations of 10–100 per liter are most frequently observed from *Krämer et al*. [2009], as shown in Figure 3. Our MMF results from LP and LPHI suggest that even though homogeneous nucleation is favored at low temperatures, high Ni values (1000/L) are infrequent. This result also indicates that when nucleation is linked to supersaturation, vertical velocity, and aerosol number concentrations in MMF, the preexisting ice problem in traditional GCMs is improved. This improvement is attributed to both the MMF model structure and the aerosol-enabled ice nucleation scheme; the sub-GCM-grid variability of important variables provided by the embedded CRMs is strongly coupled with the ice nucleation parameterization. At higher temperatures (>210 K), the median value from LPHI decreases with increasing temperature and the number is lower than the observed median Ni value reported from *Heymsfield et al*. [2013].

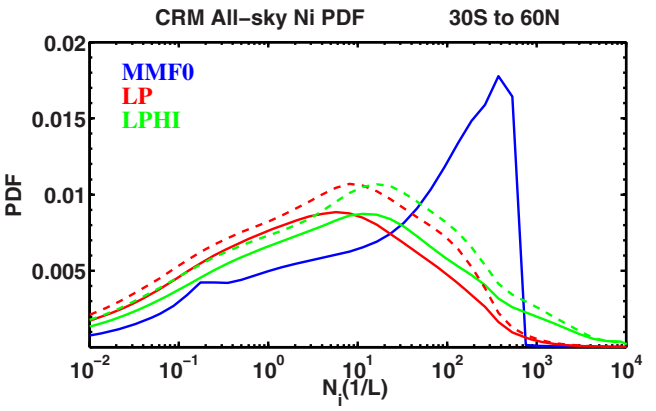

Figure 4. Probability distribution function (PDF) of all sky Ni from 30°S to 60°N over 150–300 hPa pressure levels from CRM-grid output. Dashed green and red curves are for Dcs = 250 μm cases.

Figure 4 shows the all-sky Ni between 150 and 300 mbar and from 30°S to 60°N latitude band. The MMF0 model predicts a high peak of Ni distribution around 200–300/L. In LP cases, Ni peaks higher for the Dcs = 250μm cases and HI cases (between 10/L and 100/L). The observed in-cloud Ni distribution from the SGP site suggests

that the most frequently observed Ni is in the range of about 10–200/L with a peak around 10/L [*Liu et al*., 2012a], which is also consistent with the new MMF modeled peak of the Ni distribution over SGP site (not shown).

3.3. Ice Supersaturation and Freezing Mechanism

The relative humidity in the atmosphere is a key driver of ice initiation. In order to form ice in clear sky, a certain RHi threshold has to have been reached through dynamical processes such as upward vertical motion. Homogeneous freezing has a higher RHi threshold to form ice (around 150%) than heterogeneous freezing with a foreign substance presented as IN (120–140%) [*Pruppacher and Klett*, 1997]. Meanwhile, once ice particles are formed, they grow by consuming surrounding water vapor; therefore the value of in-cloud RHi is also determined by vapor depositional growth after ice initiation [*DeMott et al*., 1994; *Comstock*, 2004; *Lohmann et al*., 2008]. Thus, one can infer the relative importance of freezing modes from the value and distribution of RHi [*Haag et al*., 2003].

3.3.1. Ice Supersaturation Distribution

Sustained high supersaturation over ice and low ice crystal concentrations in low temperature cirrus clouds have been observed or derived from both in situ and satellite observations [e.g., *Spichtinger et al*., 2003; *Gettelman et al*., 2006; *Lawson et al*., 2008; *Krämer et al*., 2009]. A number of studies have proposed that low ice concentrations result from the dominance of heterogeneous freezing or from dynamical mechanisms [*Barahona and Nenes*, 2011; *Spichtinger and Krämer*, 2013]. Earlier numerical studies by *DeMott et al*. [1994, 1997] simulated cirrus initiation with both homogeneous and heterogeneous freezing, assuming an abundance of effective ice nuclei (IN) in the upper troposphere. With the aid of recent aircraft measurements and satellite observations, *Jensen et al*. [2010] pointed out that the onset of heterogeneous nucleation is likely the most obvious reason to explain observed low ice concentrations and broad size distributions of ice particles.

As pointed out in the Introduction, conventional GCMs, with a time step typically comparable to or longer than 10 min, have difficulty capturing ice nucleation events with time scales ranging from seconds to minutes [*Khvorostyanov et al*., 2006; *Kärcher and Burkhardt*, 2008]. Moreover, observations of relative humidity in cirrus from aircraft or satellite could be taken during various stages of cirrus development. *Spichtinger et al*. [2004] point out that a substantial fraction of sampled RHi are in fact in the transition phase to phase equilibrium. Therefore, it is more meaningful to compare RHi simulated from the MMF CRM grid data to observation, given the finer spatial and temporal scales used in the CRMs (4 km grid spacing and 20 s time step).

In our study we evaluate the occurrence frequency of all-sky RHi at 150– 300 hPa model levels and from 30°S to 60°N, and compare the simulated results (see Figure 5, left plot for CRM-grid output and right plot for GCM-grid output) to upper troposphere humidity observations from the MOZAIC project and the AIRS satellite [*Gierens et al*., 1999; *Gettelman et al*., 2006]. Note that although both data sets have been used for a number of model evaluations [i.e., *Gettelman et al*., 2010; *Liu et al*., 2012a], the observations from both independent sources do not match each other, especially for ice supersaturated conditions. The in situ measurements (MOZAIC) are believed to overestimate RHi values due to sample bias [*Lohmann et al*., 2008], while the satellite measurements tend to miss thin cirrus and have a large uncertainty about 20% [*Liu et al*., 2012a]. Nevertheless, both data sets exhibit an exponential decrease of RHi above 100%.

Figure 5a shows the 3 hourly instantaneous output from CRM grid points: the original MMF0 underestimates the frequency of ice supersaturation compared to both observational data sets. Instead, it predicts a higher frequency of ice saturation, which is associated with a lower ice initiation threshold (108% of RHi) and larger ice crystal number concentrations (a peak of 200–300/L as shown in Figure 4). The large amount of nucleated ice quickly depletes the excess water vapor, which brings the system to equilibrium efficiently. Both LP and LPHI simulate the tail of the relative humidity PDF as in the observations. In these two cases, Ni peaks around 10 per liter, and ice begins to form only when either the homogenous or heterogeneous freezing threshold is reached. At RHi around 160%, there is a sudden decrease of frequency, which indicates fast vapor depletion by larger number of ice crystals produced by the homogeneous freezing. When a higher Dcs value is considered, the Ni peak slightly shifts to larger values and with higher frequency, but the change of RHi PDF is negligible, except that RHi frequency at ice saturation is slightly higher, because of more efficient removal of ice supersaturation from higher ice crystal number concentration (not shown). It is noteworthy that for GCM grid output (Figure 5b), in contrast to MMF results, CAM5 simulates a prominent

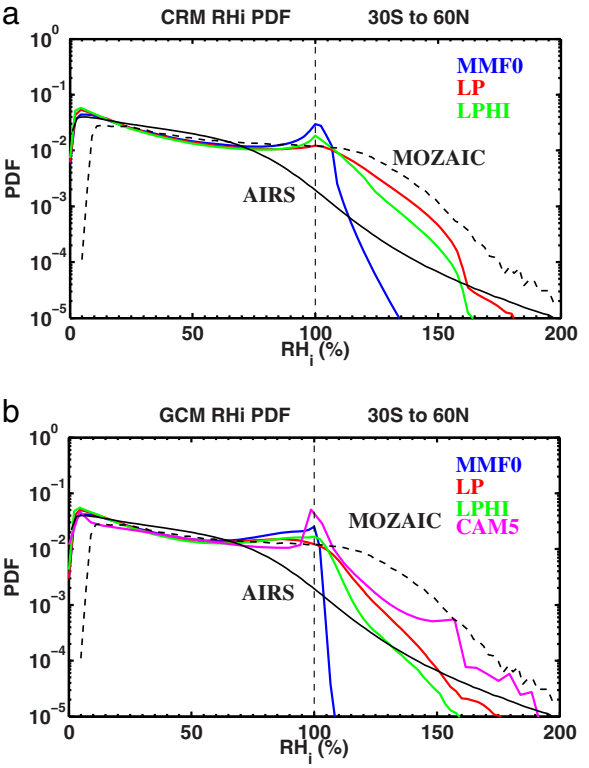

Figure 5. Probability distribution function (PDF) of all sky relative humidity over ice (RHi) over 150–300 hPa atmosphere from 30°S to 60°N from simulations: (a) the PDF of RHi which is instantaneously outputted every 3 h from CRM grids from MMF0, LP, LPHI simulations, (b) similar to Figure 5a, except that outputs are from GCM grids and results are compared with that from CAM5 simulation (magenta). Solid and dashed black lines are upper troposphere humidity observations from the Atmospheric Infra-Red Sounder (AIRS) satellite and from the Measurements of Ozone, Water Vapor, Carbon Monoxide and Nitrogen Oxides by Airbus In-Service Aircraft (MOZAIC).

peak at ice saturation, which does not appear in these two observational data sets. The peak is most likely caused by the fact that grid-mean saturation ratio is used for calculating vapor deposition at the large time step of CAM5. All of the MMF cases have a narrower RHi distribution from the GCM grid output than from the CRM grid.

Both inside and outside of cirrus, observed RHi values are positively skewed at lower temperatures as reported for the SPARTICUS campaign [*Zhang et al*., 2013], as well as the earlier study by *Krämer et al*. [2009]. Figure 6 shows the joint PDF of RHi and temperature in the upper troposphere (150–300 hPa) from MMF0, LP and LPHI. RHi in MMF0 is centered around ice saturation and is lower than in both LP cases. For the LP cases, simulated bivariate PDF of RHi and temperature approximately follows the slope of relative humidity over ice threshold of homogenous nucleation (calculated from *Koop et al*. [2000]), which agrees with the observed relative humidity distribution from SPARTICUS [*Zhang et al*., 2013, Figure 6]. LP predicts a higher frequency of ice supersaturation than LPHI due to lower ice crystal number concentrations (Figure 5), which leads to longer vapor relaxation time and higher residual supersaturation. At the same time, a higher frequency of high RHi is simulated in the Southern Hemisphere (SH) mainly because of lower simulated temperature over the midlatitude SH. Note here that for the tropics, the banded occurrence frequency over four temperature regions is caused by a horizontally homogeneously distributed temperature, limiting the range of temperature at a given model vertical level.

3.3.2. Interhemispheric and Seasonal Variations

In this section, we present the interhemispheric and seasonal variation of ice supersaturation and ice nucleation simulated from MMF. Figure 7 shows the MMF simulated seasonal variation of mean supersaturation (Si) and the supersaturation frequency over the SH midlatitudes, tropics and the Northern Hemisphere (NH) midlatitudes in the upper troposphere (from 300 to 150 hPa). MMF0 simulates the lowest mean Si over all seasons and latitude bands than LP cases, while the Si frequencies are rather similar for these cases. The tropics in general have the highest Si occurrence, and the NH has a lower Si occurrence than SH. Although the inter-hemispheric asymmetry agrees with earlier in situ [i.e., *Ovarlez et al*., 2002] and satellite observations [*Gettelman et al*., 2006; *Kahn et al*., 2009], the simulations tend to underestimate Si frequency in the tropics and to overestimate it in both the SH and NH midlatitudes, when compared to ice supersaturation measurement from Microwave Limb Sounder (MLS) satellite data [*Spichtinger et al*., 2003].

Si observations from the MLS at the 147 hPa and 215 hPa pressure levels indicate that the mean frequency of Si is about 19% and 6% for each level in the tropics and about 2% in the mid latitude SH and NH. The data derived from MOZAIC, however, suggest a 10% occurrence of Si during data sampling period over NH, which is comparable with MMF results [*Spichtinger et al*., 2003; *Lohmann et al*., 2008; *Wang and Penner*, 2010].

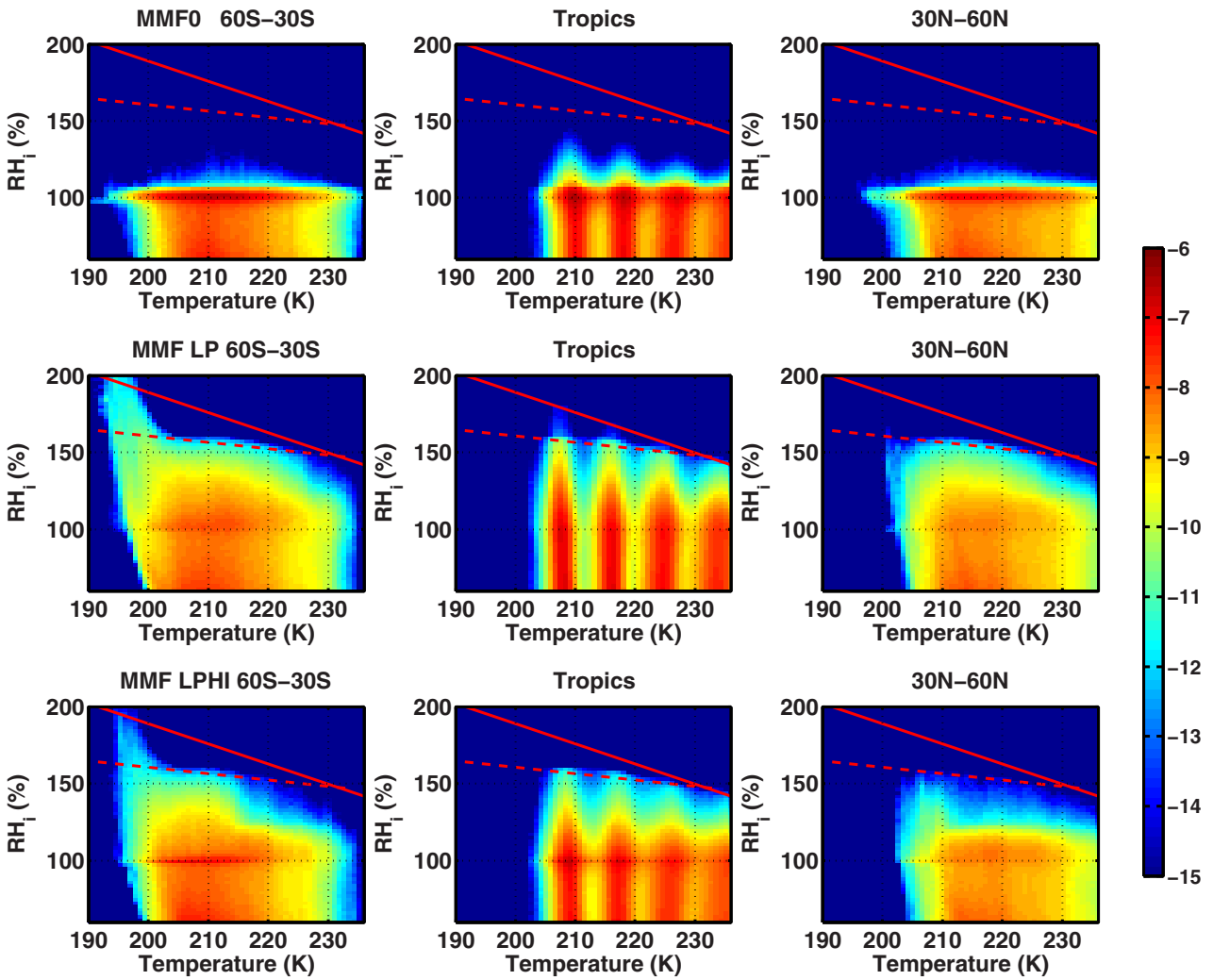

Figure 6. Simulated joint probability density function (PDF) of RHi (%) and temperature (K) in the upper troposphere (150–300 hPa) of September, October, November (SON). The simulated PDFs are computed from 1 year of instantaneous 3 hourly model output and partitioned into three regions: Midlatitude Southern Hemisphere ((left) from 60°S to 30°S), Tropics ((middle) from 30°S to 30°N and midlatitude Northern Hemisphere ((right) from 30°N to 60°N). Three rows are for three simulations: MMF0, LP, and LPHI from top to bottom. The solid red line indicates water saturation and the dashed red line shows the RHi threshold for homogeneous freezing of liquid solution calculated according to *Koop et al.* [2000].

The modeling study of *Haag et al.* [2003] pointed out that homogeneous nucleation of supercooled solution aerosols corresponds to high Si in SH, while the onset of heterogeneous nucleation on IN which suppresses homogeneous nucleation explains the lower Si in the NH. On the other hand, *Gettelman et al.* [2006] suggested that temperature variation is a control of the inter-hemispheric difference of RHi derived from AIRS data sets. In our case, all MMF simulations with or without explicit linking of ice nucleation to aerosols have an asymmetric hemispheric Si distribution. Although it underestimates the Si values, MMF0 with a simple temperature-dependent ice nucleation scheme simulates an overall higher Si frequency in the SH, which implies that temperature may be the dominant control in determining the occurrence of Si. Generally, all three MMF cases predict larger RHi frequency in the midlatitude winter hemisphere than that of summer hemisphere (In LPHI case, at DJF RHi frequency in the NH is slightly smaller than SH, but at JJA RHi frequency in the SH is much larger compared to the NH), which agrees with AIRS data sets [*Kahn et al.*, 2009].

Figure 8 shows the in-cloud ice production rate and occurrence frequency from homogeneous and heterogeneous nucleation for LP (a) and LPHI (b) cases. In general, homogeneous nucleation has a greater ice production rate but lower occurrence frequency than heterogeneous nucleation in cloud. High ice production promoted by homogeneous nucleation tends to quickly deplete available water vapor and suppresses nucleation. In contrast, the production rate from heterogeneous nucleation is low, which favors further ice nucleation due to less efficient water vapor depletion. In the NH, heterogeneous freezing happens more

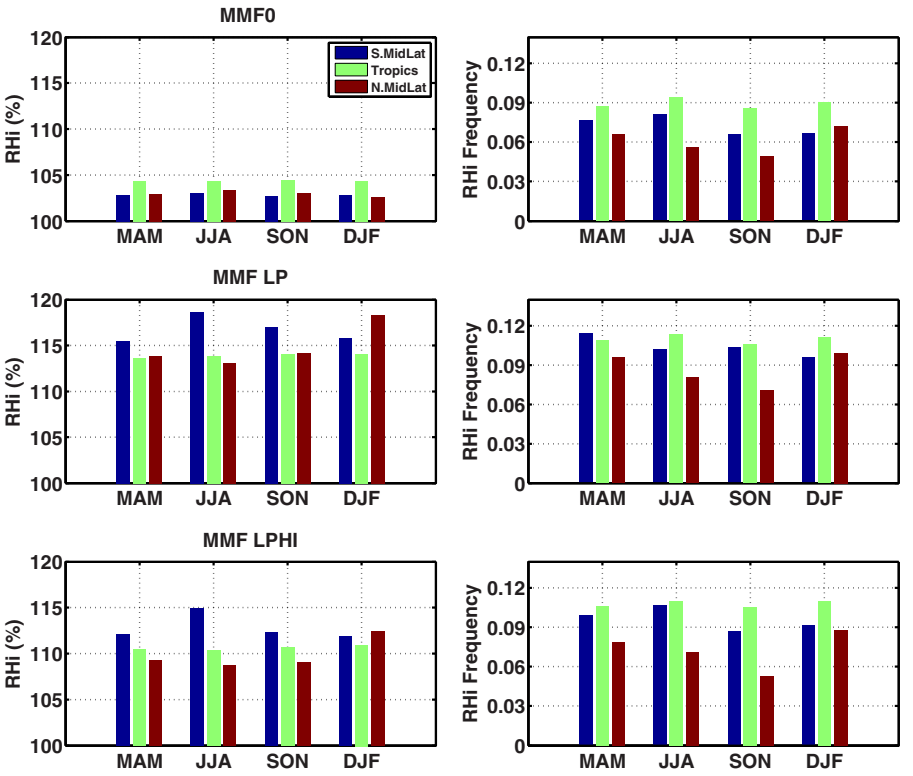

Figure 7. (left) Simulated mean ice supersaturation and (right) its occurrence frequency over midlatitude Southern Hemisphere, Tropics and midlatitude Southern Hemisphere at upper troposphere (150–300 hPa) in four seasons: spring = MAM: March, April, May; summer = JJA: June, July, August; autumn = SON: September, October, November, and winter = DJF: December, January, February. Results are from three model simulations: (top) MMF0, (middle) LP, and (bottom) LPHI.

often, given the more abundant dust IN compared to the SH in boreal spring and fall. In the LPHI case, homogeneous ice production rates are 2–3 orders magnitude higher compared to LP, due to the large number of small sulfate aerosols allowed to form ice, while the nucleation frequency is even lower because of the high ice production rate. Due to much higher concentrations of dust particles that can nucleate ice, the ice production rate from heterogeneous nucleation in LPHI simulation is also high. For the tropics and SH, the heterogeneous nucleation frequency is higher than in LP, while in the NH it is often lower (except for winter). Higher heterogeneous nucleation rates in this case also have a similar suppression effect as homogeneous nucleation so that ice supersaturation is lower in LPHI (Figure 7). In both the LP and LPHI cases, the frequency of heterogeneous freezing mode is higher than homogeneous freezing over all seasons and latitude bands. Overall, heterogeneous freezing is found to be the dominant nucleation mechanism for ice production in terms of ice nucleation frequency in these simulations. We note here that the dominant nucleation mechanism could be different if different heterogeneous ice nucleation parameterizations are used.

3.4. Annual Global Mean Diagnostics

A summary of global annual mean cloud parameter diagnostics from all the runs is provided in Table 2. We also note that compared to the finer grid MMF0 simulation ($1.9^\circ \times 2.5^\circ$) performed by *Wang et al*. [2011b], the coarser horizontal resolution 4°x5° run provides close agreement in global mean cloud parameters (see Table 2). The simulated global mean shortwave cloud forcing (SWCF) and longwave cloud forcing (LWCF) are compared to those derived from satellite products ERBE and CERES [*Loeb et al*., 2009]. When the LP05 scheme is applied, the simulated SWCF and LWCF from all cases are weaker than that from MMF0, especially the LP case which under-predicts both cloud forcing due to the lowest column ice number concentration and lowest high cloud fraction (also see Figure 9). Although LWCF predicted by all configurations of the new MMF is weaker than that derived from ERBE and CERES (from 27 to 31 Wm^{-2}), these values are

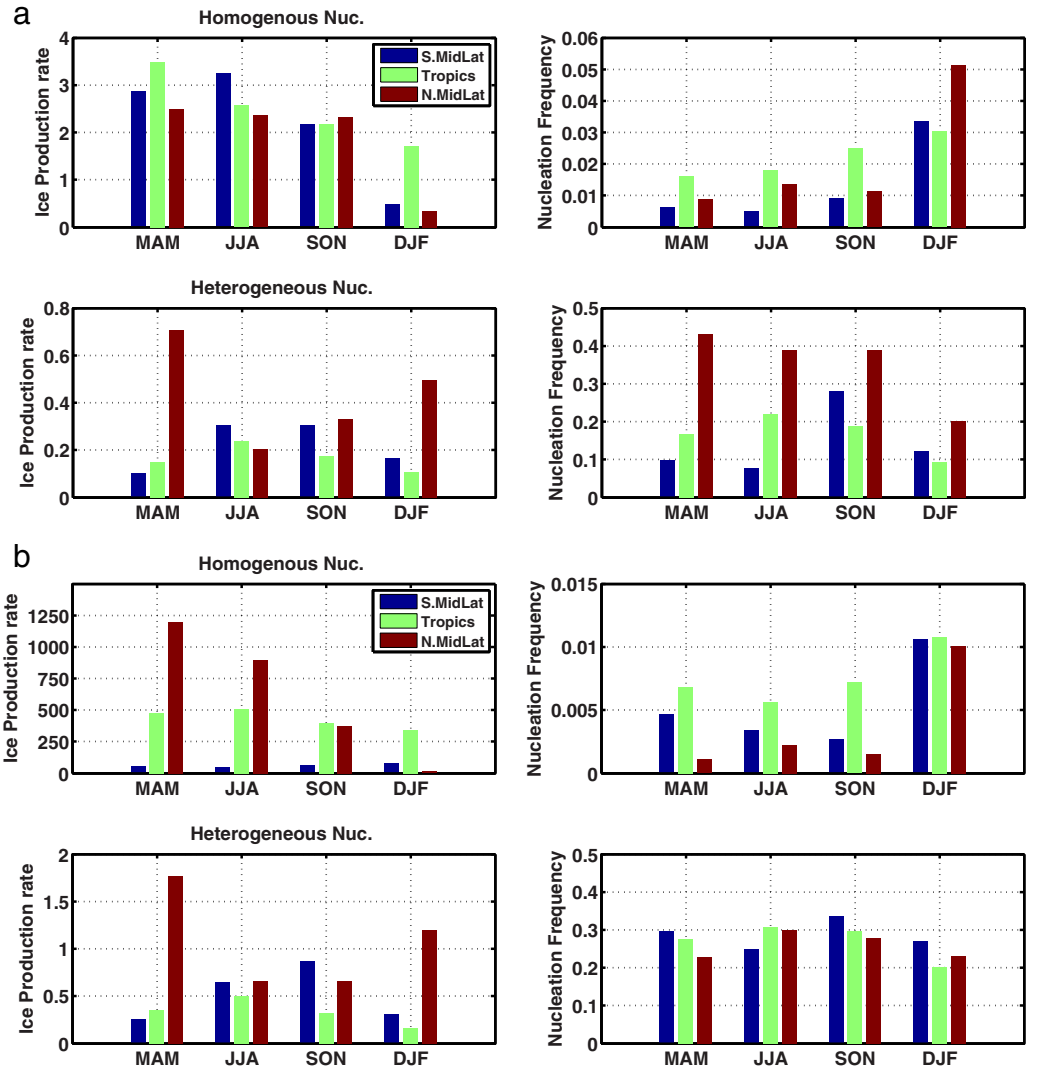

Figure 8. Contributions of homogeneous and heterogeneous ice nucleation to crystal production at upper troposphere (150–300 hPa) in four seasons. Left plots show the production rates, which is in the unit of number of crystals per liter per model time step (i.e., 20 s). Right plots show the frequency of occurrence of ice nucleation through homogeneous and heterogeneous pathways respectively. (a) LP case and (b) LPHI case.

comparable to the LWCF derived from TOVS retrievals (about 22 Wm^{-2}, cited by *Lohmann et al.* [2007] and *Hendricks et al.* [2011]), except for the case LP.

Figure 9 shows the annual and zonal mean SWCF (upper) and LWCF (lower) from the model simulations and from satellite retrievals using CERES [*Wielicki et al.*, 1996]. Differences between simulations for SWCF are less noticeable than LWCF. This result is expected since LWCF is more sensitive to how ice processes are treated in clouds. The magnitude of LWCF can be under-predicted by more than 10 Wm^{-2} over midlatitude SH and NH. This bias is also found in other CAM5 studies [e.g., *Liu et al.*, 2012a].

The simulated ice water path (IWP) depends strongly on the critical diameter (Dcs) for autoconversion of cloud ice to snow. By increasing Dcs from 125 to 250 μm, IWP increases by more than a factor of 3, and high-cloud fraction rises by 30%. With a higher threshold size for ice-snow conversion, more ice particles remain in the cloud ice category, and therefore column integrated ice number concentration (NUMI) increases accordingly. However, a more significant factor that controls NUMI is the aerosol configuration. When a high aerosol setting is applied in the ice nucleation scheme, global mean NUMI simulated by the MMF (LP versus LPHI, LP250 versus LPHI250) is up to about 4 times greater than that using the default aerosol setting. The ice nucleation scheme has a negligible effect on the prediction of LWP in the MMF.

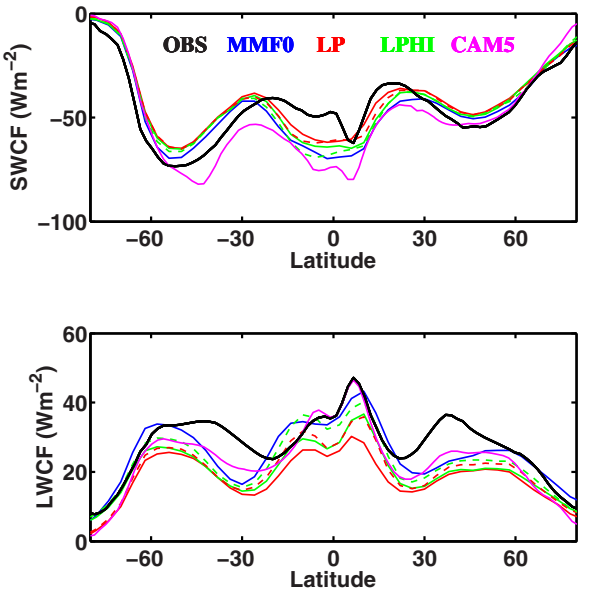

Figure 9. Annual and zonal mean distributions of shortwave cloud forcing (SWCF), longwave cloud forcing (LWCF) from different model simulations. Black line is from observations. Solid color lines for Dcs=125 μm and dashed color lines for Dcs=250 μm.

The IWP and cloud ice water content (IWC) are also compared with the derived data sets from CloudSat level-2C ice cloud property product (2C-ICE) [*Deng et al*., 2013]. The 2C-ICE data provide vertically resolved ice cloud properties such as IWC, effective radius and extinction coefficient, obtained by combining CloudSat and CALIPSO at the CloudSat horizontal and vertical resolutions based on an optimal estimation framework. Because of the use of CALIPSO in the 2C-ICE product described above, the derived IWP/IWC will have more sensitivity to thin/cirrus ice clouds. The CloudSat 2C-ICE retrieval algorithm uses parameterized radar signals in ice cloud volumes below the CloudSat radar detection threshold as an extra constraint, which provides better agreement with in situ data than other products (i.e., DARDAR (raDAR/liDAR) [*Hogan*, 2006; *Delanoë and Hogan*, 2008, 2010; *Deng et al*., 2013].

In order to make direct comparisons of cloud/floating ice content between the observations and model, *Li et al*. [2012] removed the contribution from precipitating and convective cloud hydrometeors. This method excludes all the retrievals in any profile that are flagged as precipitating at the surface and any retrieval within the profile whose cloud type is classified as "deep convection" or "cumulus" (based on CloudSat 2B-CLDCLASS and 2C-PRECIP-COLUMN data: http://www.cloudsat.cira.colostate.edu/dataSpecs.php). By excluding these portions of the ice mass, an estimate of the cloud-only portion of the IWP/IWC is estimated for model evaluation. Details and validation of this product can be found in several studies [*Deng et al*., 2010; *Li et al*., 2012; *Deng et al*., 2013].

Figure 10 shows annual mean meridional distributions of simulated and retrieved IWP (left) and vertical profiles of IWC (right); the top plots show cloud ice and the bottom plots the total ice water (ice+snow+graupel). For the cases with Dcs = 125 μm (solid lines), MMF0 predicts the highest cloud IWP over all latitudes. LP and LPHI predict similar cloud IWP except over the SH high latitudes due to substantially higher sulfate concentrations in the LPHI case. Cloud IWP depends heavily on Dcs. With Dcs = 250 μm, the simulated global mean cloud IWP from the LP05 scheme (24.4 Wm^{-2} for LP250 and 26.4 Wm^{-2} for LPHI250) increases by more than a factor of three and agrees well with the retrieval (26.5 Wm^{-2}). However, cloud IWP deviates from the retrieval at certain latitudes, e.g., SH middle latitudes, which is a bias present in all MMF simulations, including MMF0. Similarly, with Dcs = 250 μm, the vertical profile of cloud IWC matches the retrieval; peak values are located between 600 and 200 hPa, and maxima are slightly smaller than observed values. In the lower atmosphere, IWC deviates from the retrieval. It is noted that the satellite retrieval is subject to larger uncertainty there, due to the difficulty in separating ice from liquid hydrometeors below the freezing level [*Li et al*., 2012]. When all ice phase hydrometers are considered (the bottom plots in Figure 10), the high Dcs cases have about 10% to 20% higher total IWP than the other cases. Thus, total IWP has a lower sensitivity to Dcs than cloud IWP.

4. Summary Discussion and Conclusion

Cirrus clouds have important effects on Earth's energy budget and hydrologic cycle. Representing cirrus clouds is challenging in conventional GCMs due to the coarse spatial and temporal model resolutions at which the subgrid vertical velocity and relative humidity that are required for ice nucleation calculation are diagnosed.

In this study, an aerosol-dependent ice nucleation scheme following *Liu and Penner* [2005] (LP05) has been implemented into an aerosol-enabled Multiscale Modeling Framework (PNNL MMF). By explicitly calculating ice initiation based on CRM-scale temperature, humidity, vertical velocity, and aerosol number concentrations,

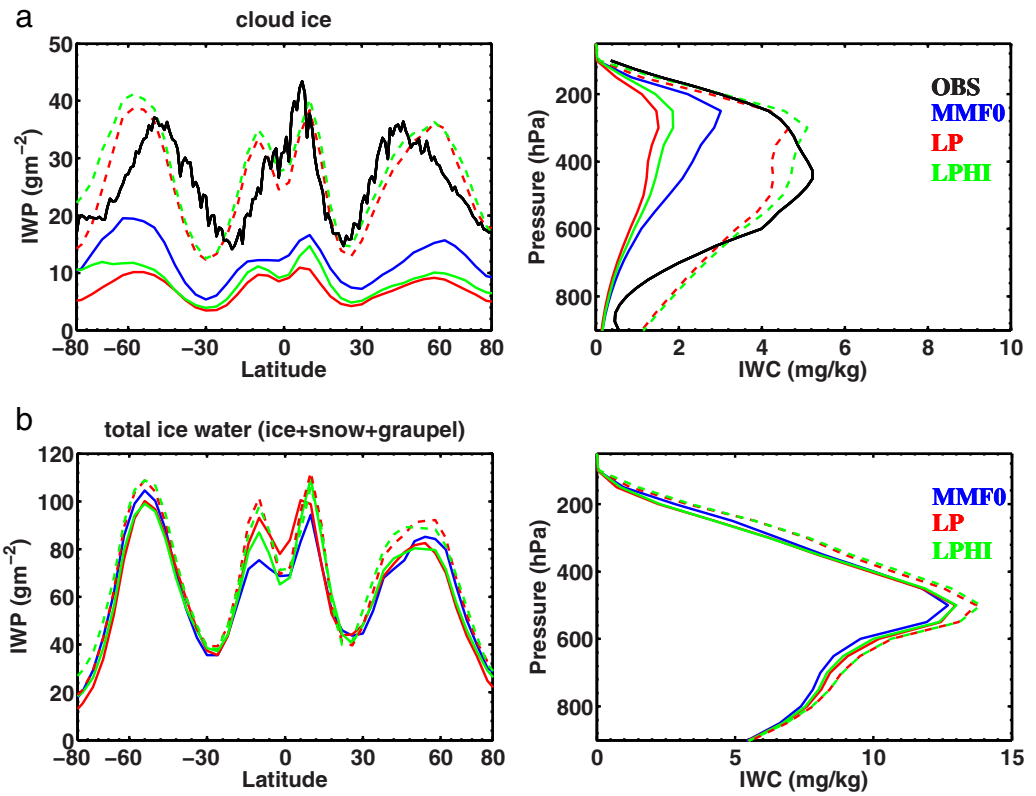

Figure 10. Simulated IWP/IWC in comparison with data sets derived from CloudSat 2C-ICE (black curve). (left) Zonally averaged IWP, and (right) vertical IWC profiles. (top) Cloud ice water and (bottom) total ice water. MMF0 results are in blue, LP in red and LPHI in green. Solid color curves for Dcs=125 μm and dashed color curves for Dcs=250 μm.

the representation of cirrus clouds has been improved compared to that of the original version of this MMF (MMF0). The MMF model with the new ice nucleation scheme simulates the frequent occurrence of high ice supersaturation and low ice number concentration (10–100/L) observed in the upper troposphere. The MMF0 model failed to simulate the high occurrence of ice supersaturation due to overprediction of the ice nucleation rate from the simple temperature-dependent ice nucleation scheme. The key process explaining the low ice number modeled with the new MMF is that the vapor depletion has been better simulated in a more realistic ice nucleation scheme. Homogeneous freezing happens much less frequently, due to fast vapor depletion that inhibits further nucleation after large amounts of ice are produced. The preexisting ice problem evident in some traditional GCMs [*Hendricks et al.*, 2011] is also improved, due to strong coupling of the supersaturation and vertical velocity produced by the embedded CRMs with the ice nucleation scheme.

The improved MMF with the LP nucleation scheme simulates the high frequency of ice supersaturation that is found in both in situ and satellite observational data sets. The high occurrence of ice saturation simulated by CAM5, which is inconsistent with observations, is not evident in the MMF simulations. Modeled ice supersaturation is positively skewed at lower temperatures, closely following the saturation threshold for homogeneous nucleation. Our results also suggest that the MMF is inherently better suited to simulate processes with a fairly short time scale (less than that of typical GCM time steps), such as ice nucleation.

The global distribution of ice supersaturation and ice production rate from heterogeneous and homogeneous nucleation mechanisms vary with latitude bands and time of the year. The MMF models, including MMF0 with ice nucleation dependent on temperature only, simulate high supersaturation in the SH and winter hemisphere, which agrees with observations. This suggests that temperature is the dominant control of the interhemispheric supersaturation distribution asymmetry.

The MMF LP and LPHI simulations suggest that higher homogeneous ice production rates occur with low nucleation frequency, and lower heterogeneous ice production rates occur with high frequency. High rates of ice production, either from homogeneous or heterogeneous nucleation (when IN are abundant),

consume water vapor rapidly and have a suppression effect on further nucleation. In general, heterogeneous nucleation frequency is higher than homogeneous nucleation over all seasons and latitude bands.

The sensitivity of the model to the aerosol distribution (for aerosols that can nucleate ice) and ice nucleation parameterization has been tested in this work. The geographical distribution of atmospheric ice can change significantly using different ice nucleation schemes. The modeled ice number is also sensitive to the critical cutoff made for the aerosol size distribution as an input for ice nucleation. When only larger sulfate particles (diameter > 0.1 μm) and coarse mode dust are allowed to form ice (which is the default condition for CAM5), both SWCF and LWCF are under-estimated by the MMF. In addition, the modeled cloud ice number is sensitive to the cloud ice-to-snow autoconversion threshold diameter (Dcs). The ice water content/path increases by more than a factor of 3 by increasing Dcs from 125 to 250 μm. The mean cloud IWC matches satellite-derived 2C-ICE CloudSat data with Dcs $=250$ μm, while the model simulated total ice water path is not sensitive to the specification of Dcs. *Zhang et al*. [2013] also suggested that the Dcs value of 250 μm produces a CAM5 simulation that matches best with the SPARTICUS measurements. The choice of the autoconversion threshold diameter in atmospheric models requires further observational justification. *Schmitt and Heymsfield* [2014] analyzed two particle imagery data sets collected from high-resolution aircraft particle imaging probes and found that the separation between ice and snow occurs at 150 and 250 μm for each data set.

In order to produce realistic ice numbers in the default version of CAM5 [*Gettelman et al*., 2010], several constraints have to be made for the LP nucleation scheme: subgrid vertical velocity has to be smaller than 0.2 m s^{-1}; only sulfate aerosol particles in Aitken mode with diameter greater than 0.1 μm and only dust in coarse mode can form ice; and a scaling factor of 1.2 is used for grid box relative humidity to implicitly represent humidity variation over the grid box. Increasingly many lines of evidence [*Zhang et al*., 2013; *Shi et al*., 2014] have shown that some of these limitations may not be physical and not necessary if the physical processes are better treated. Our study shows that these constraints can be removed for LP in MMF. A detailed comparison of other microphysical processes between CAM5 and MMF will be helpful for further clarifying model differences.

Although MMF shows improvement on simulating ice nucleation over conventional GCMs, there are issues remaining with the MMF approach. The time step of 20 s in the embedded cloud resolving models may not be sufficient in simulating the ice nucleation process, especially for homogeneous nucleation under high vertical velocities. On the other hand, the fixed time step may cause issue too. Although most cloud resolving model studies are using fixed time ranging from 0.5 s to 20 s as model time step or microphysics subtime step [*Tao et al*., 2012; *Muhlbauer et al*., 2014], ice nucleation parameterizations can be sensitive to the prescribed time step [*Spichtinger and Gierens*, 2009]. One of the possible solutions to further improve the simulations of ice processes in MMF may be to use an adaptive time step (as a function of variables, such as vertical velocity, T, humidity and aerosol numbers) for the microphysics processes (nucleation, depositional growth and sedimentation), similar to those proposed by *Spichtinger and Gierens* [2009] and *Eidhammer et al*. [2009].

In this study, cirrus clouds were investigated exclusively. The parameterization of mixed phase ice nucleation through deposition and condensation/immersion freezing should be investigated in future work. In addition, it will be useful to apply a satellite simulator to the MMF output following *Zhang et al*. [2008] and *Marchand and Ackerman* [2010], thus facilitating comparison with satellite observations.

Acknowledgments
This research was supported by the Center for Multiscale Modeling of Atmospheric Processes (CMMAP), a National Science Foundation (NSF) Science and Technology Center managed by Colorado State University under Cooperative Agreement ATM-0425247. C. Zhang wants to thank Gabe Kooperman and Mike Pritchard for insightful discussions. M. Wang was supported by the DOE Office of Science, Decadal and Regional Climate Prediction using Earth System Models (EaSM) program. PNNL is operated by Battelle for the DOE under Contract DE-AC06–76RLO 1830. K. Zhang acknowledges the support from the U.S. Department of Energy Atmospheric System Research Program. We thank the anonymous reviewers for their extremely conscientious and constructive comments and suggestions, which greatly improved the manuscript. Our research used the Extreme Science and Engineering Discovery Environment (XSEDE), which is supported by National Science Foundation grant number OCI-1053575. We also would like to acknowledge high-performance computing support from Yellowstone (ark:/85065/d7wd3xhc) provided by NCAR's Computational and Information Systems Laboratory, sponsored by the National Science Foundation. The original PNNL MMF model is available through the NCAR CESM repository at: https://svn-ccsm release.cgd.ucar.edu/model_development_releases/spcam2_0-cesm1_1_1. The model with updated ice nucleation is available upon request to C. Zhang.

References

Barahona, D., and A. Nenes (2009), Parameterizing the competition between homogeneous and heterogeneous freezing in cirrus cloud formation monodisperse ice nuclei, *Atmos. Chem. Phys.*, *9*(2), 369–381.

Barahona, D., and A. Nenes (2011), Dynamical states of low temperature cirrus, *Atmos. Chem. Phys.*, *11*, 3757–3771.

Cantrell, W., and A. Heymsfield (2005), Production of ice in tropospheric clouds: A review, *Bull. Am. Meteorol. Soc.*, *86*, 795–807.

Comstock, J. M. (2004), Evidence of high ice supersaturation in cirrus clouds using ARM Raman lidar measurements, *Geophys. Res. Lett.*, *31*, L11106, doi:10.1029/2004GL019705.

Cooper, W. A. (1986), Ice Initiation in Natural Clouds. *Meteorological Monographs*, *21*, 29–32, doi:http://dx.doi.org/10.1175/0065-9401-21.43.29.

Cziczo, D. J., et al. (2013), Clarifying the dominant sources and mechanisms of cirrus cloud formation, *Science N. Y.*, *340*(6138), 1320–1324.

Delanoë, J., and R. J. Hogan (2008), A variational scheme for retrieving ice cloud properties from combined radar, lidar, and infrared radiometer, *J. Geophys. Res.*, *113*, D07204, doi:10.1029/2007JD009000.

Delanoë, J., and R. J. Hogan (2010), Combined CloudSat-CALIPSO-MODIS retrievals of the properties of ice clouds, *J. Geophys. Res.*, *115*, D00H29, doi:10.1029/2009JD012346.

DeMott, P. J., M. P. Meyers, and W. R. Cotton (1994), Parameterization and impact of ice initiation processes relevant to numerical model simulations of cirrus clouds, *J. Atmos. Sci.*, *51*, 77–90.

DeMott, P. J., D. C. Rogers, and M. Kreidenweis (1997), The susceptibility of ice formation in upper tropospheric clouds to insoluble aerosol components, *J. Geophys. Res.*, *102*(D16), 19,575–19,584, doi:10.1029/97JD01138.

DeMott, P. J., et al. (2010), Predicting global atmospheric ice nuclei distributions and their impacts on climate, *Proc. Natl. Acad. Sci. U. S. A.*, *107*(25),11,217–11,222.

Deng, M., G. G. Mace, Z. Wang, and R. P. Lawson (2013), Evaluation of several A-Train ice cloud retrieval products with in situ measurements collected during the SPARTICUS campaign, *J. Appl. Meteorol. Climatol.*, *52*(4), 1014–1030.

Deng, M., G. G. Mace, Z. Wang, and H. Okamoto (2010), Tropical composition, cloud and climate coupling experiment validation for cirrus cloud profiling retrieval using cloudsat radar and calipso lidar, *J. Geophys. Res.*, *115*, D00J15, doi:10.1029/2009JD013104.

Easter, R. C., and L. K. Peters (1994), Binary homogeneous nucleation: Temperature and relative humidity fluctuations, nonlinearity, and aspects of new particle production in the atmosphere, *J. Appl. Meteorol.*, *33*, 775–784.

Eidhammer, T., P. J. DeMott, and S. M. Kreidenweis (2009), A comparison of heterogeneous ice nucleation parameterizations using a parcel model framework, *J. Geophys. Res.*, *114*, D06202, doi:10.1029/2008JD011095.

Gettelman, A., E. J. Fetzer, A. Eldering, and F. W. Irion (2006), The global distribution of supersaturation in the upper troposphere from the Atmospheric Infrared Sounder, *J. Clim.*, *19*(23), 6089–6103.

Gettelman, A., et al. (2010), Global simulations of ice nucleation and ice supersaturation with an improved cloud scheme in the Community Atmosphere Model, *J. Geophys. Res.*, *115*, D18216, doi:10.1029/2009JD013797.

Gettelman, A., X. Liu, D. Barahona, U. Lohmann, and C. Chen (2012), Climate impacts of ice nucleation, *J. Geophys. Res.*, *117*, D20201, doi: 10.1029/2012JD017950.

Gierens, K. (2003), On the transition between heterogeneous and homogeneous freezing, *Atmos. Chem. Phys.*, *3*(2), 437–446.

Gierens, K., U. Schumann, M. Helten, H. Smit, and A. Marenco (1999), A distribution law for relative humidity in the upper troposphere and lower stratosphere derived from three years of MOZAIC measurements, *Ann. Geophys.*, *1226*, 1218–1226.

Grabowski, W. (2001), Coupling cloud processes with the large-scale dynamics using the Cloud-Resolving Convection Parameterization (CRCP), *J. Atmos. Sci.*, *58*(9), 978–997.

Gustafson, J. W., L. Berg, R. Easter, and S. Ghan (2008), The explicit-cloud parameterized-pollutant hybrid approach for aerosol–cloud interactions in multiscale modeling framework models: Tracer transport results, *Environ. Res. Lett.*, *3*(2), 025 005.

Haag, W., B. Kärcher, J. Strom, A. Minikin, U. Lohmann, J. Ovarlez, and A. Stohl (2003), Freezing thresholds and cirrus cloud formation mechanisms inferred from in situ measurements of relative humidity, *Atmos. Chem. Phys. Discuss.*, *3*(3), 3267–3299.

Hendricks, J., B. Kärcher, and U. Lohmann (2011), Effects of ice nuclei on cirrus clouds in a global climate model, *J. Geophys. Res.*, *116*(D18), D18206, doi:10.1029/2010JD015302.

Heymsfield, A. J., C. Schmitt, and A. Bansemer (2013), Ice cloud particle size distributions and pressure-dependent terminal velocities from in situ observations at temperatures from 0° to −86°C, *J. Atmos. Sci.*, *70*, 4123–4154.

Hogan, R. J. (2006), Fast approximate calculation of multiply scattered lidar returns, *Appl. Opt.*, *45*, 5984–5992.

Hoose, C., and O. Möhler (2012), Heterogeneous ice nucleation on atmospheric aerosols: A review of results from laboratory experiments, *Atmos. Chem. Phys.*, *12*, 9817–9854.

Hoose, C., J. E. Kristjánsson, J.-P. Chen, and A. Hazra (2010), A classical-theory-based parameterization of heterogeneous ice nucleation by mineral dust, soot, and biological particles in a Global Climate Model, *J. Atmos. Sci.*, *67*, 2483–2503, doi:10.1175/2010JAS3425.1.

IPCC AR5 (2013), Working group I Contribution to the IPCC fifth assessment report (AR5), in *Climate Change 2013: The Physical Science Basis*, edited by T. F. Stocker et al., Cambridge Univ Press, N. Y.

Jensen, E., L. Pfister, T. Bui, P. Lawson, and D. Baumgardner (2010), Ice nucleation and cloud microphysical properties in tropical tropopause layer cirrus, *Atmos. Chem. Phys.*, *10*(3), 1369–1384.

Kahn, B. H., A. Gettelman, E. J. Fetzer, A. Eldering, and C. K. Liang (2009), Cloudy and clear-sky relative humidity in the upper troposphere observed by the A-train, *J. Geophys. Res.*, *114*, D00H02, doi:10.1029/2009JD011738.

Kärcher, B., and U. Burkhardt (2008), A cirrus cloud scheme for general circulation models, *Q. J. R. Meteorol. Soc.*, *134*(635), 1439–1461.

Kärcher, B., and U. Lohmann (2002), A parameterization of cirrus cloud formation: Homogeneous freezing including effects of aerosol size, *J. Geophys. Res.*, *107*(D23), 4698, doi:10.1029/2001JD001429.

Kärcher, B., J. Hendricks, and U. Lohmann (2006), Physically based parameterization of cirrus cloud formation for use in global atmospheric models, *J. Geophys. Res.*, *111*, D01205, doi:10.1029/2005JD006219.

Khairoutdinov, M., and D. Randall (2001), A cloud resolving model as a cloud parameterization in the NCAR community climate system model: Preliminary results, *Geophys. Res. Lett.*, *28*(18), 3617–3620.

Khairoutdinov, M., C. DeMott, and D. Randall (2008), Evaluation of the simulated interannual and subseasonal variability in an amip-style simulation using the CSU multiscale modeling framework, *J. Clim.*, *21*(3), 413–431.

Khvorostyanov, V. I., H. Morrison, J. A. Curry, D. Baumgardner, and P. Lawson (2006), High supersaturation and modes of ice nucleation in thin tropopause cirrus: Simulation of the 13 July 2002 Cirrus Regional Study of Tropical Anvils and Cirrus Layers case, *J. Geophys. Res.*, *111*, D02201, doi:10.1029/2004JD005235.

Koop, T., B. Luo, A. Tslas, and T. Peter (2000), Water activity as the determinant for homogeneous ice freezing in aqueous solutions, *Nature*, *406*, 611–614.

Kooperman, G., M. Pritchard, S. Ghan, M. Wang, R. Somerville, and L. Russell (2012), Constraining the influence of natural variability to improve estimates of global aerosol indirect effects in a nudged version of the community atmosphere model 5, *J. Geophys. Res.*, *117*, D23204, doi:10.1029/2012JD018588.

Kooperman, G. J., M. S. Pritchard, and R. C. J. Somerville (2013), Robustness and sensitivities of central U.S. summer convection in the super-parameterized CAM: Multi-model intercomparison with a new regional EOF index, *Geophys. Res. Lett.*, *40*, 3287–3291, doi: 10.1002/grl.50597.

Krämer, M., C. Schiller, and A. Afchine (2009), Ice supersaturations and cirrus cloud crystal numbers, *Atmos. Chem. Phys.*, *9*, 3505–3522.

Kuebbeler, M., U. Lohmann, J. Hendricks, and B. Kärcher (2013), Dust ice nuclei effects on cirrus clouds, *Atmos. Chem. Phys. Discuss.*, *13*(4), 9751–9799, doi:10.5194/acpd-13-9751-2013.

Lamarque, J. F., et al. (2010), Historical (1850–2000) gridded anthropogenic and biomass burning emissions of reactive gases and aerosols: Methodology and application, *Atmos. Chem. Phys.*, *10*(15), 7017–7039.

Lawson, R., B. Pilson, B. Baker, Q. Mo, E. Jensen, L. Pfister, and P. Bui (2008), Aircraft measurements of microphysical properties of subvisible cirrus in the tropical tropopause layer, *Atmos. Chem. Phys.*, *8*(6), 1609–1620.

Li, J.-L. F., et al. (2012), An observationally based evaluation of cloud ice water in CMIP3 and CMIP5 GCMs and contemporary reanalyses using contemporary satellite data, *J. Geophys. Res.*, *117*, D16105, doi:10.1029/2012JD017640.
Liu, X., and J. E. Penner (2005), Ice nucleation parameterization for globalmodels, *Meteorol. Z.*, *14*(4), 499–514, doi:10.1127/0941-2948/2005/0059.
Liu, X., J. E. Penner, S. J. Ghan, and M. Wang (2007), Inclusion of Ice Microphysics in the NCAR Community Atmospheric Model Version 3 (CAM3), *J. Clim.*, *20*(18), 4526–4547.
Liu, X., X. Shi, K. Zhang, E. J. Jensen, A. Gettelman, D. Barahona, A. Nenes, and P. Lawson (2012a), Sensitivity studies of dust ice nuclei effect on cirrus clouds with the Community Atmosphere Model CAM5, *Atmos. Chem. Phys.*, *12*(24), 12,061–12,079, doi:10.5194/acp-12-12061-2012.
Liu, X., et al. (2012b), Toward a minimal representation of aerosols in climate models: Description and evaluation in the Community Atmosphere Model CAM5, *Geosci. Model Dev.*, *5*(3), 709–739.
Loeb, N. G., et al. (2009), Toward optimal closure of the Earth's top-of-atmosphere radiation budget, *J. Clim.*, *22*(3), 748–766.
Lohmann, U., P. Stier, C. Hoose, S. Ferrachat, S. Kloster, E. Roeckner, and J. Zhang (2007), Cloud microphysics and aerosol indirect effects in the global climate model ECHAM5-HAM, *Atmos. Chem. Phys.*, *7*, 3425–3446, doi:10.5194/acp-7-3425-2007.
Lohmann, U., P. Spichtinger, S. Jess, T. Peter, and H. Smit (2008), Cirrus cloud formation and ice supersaturated regions in a global climate model, *Environ. Res. Lett.*, *3*(4), 045–022.
Lynch, D. (2002), Cirrus: History and definitions, in *Cirrus*, edited by D. Lynch et al., Oxford Univ. Press, N. Y.
Marchand, R., and T. Ackerman (2010), An analysis of cloud cover in multiscale modeling framework global climate model simulations using 4 and 1 km horizontal grids, *J. Geophys. Res.*, *115*, D16207, doi:10.1029/2009JD013423.
McFarquhar, G. M., G. Zhang, M. R. Poellot, G. L. Kok, R. McCoy, T. Tooman, A. Fridlind, and A. J. Heymsfield (2007), Ice properties of single-layer stratocumulus during the Mixed-Phase Arctic Cloud Experiment. 1. Observations, *J. Geophys. Res.*, *112*, D24201, doi:10.1029/2007JD008633.
Morrison, H., J. A. Curry, and V. I. Khvorostyanov (2005), A new double-moment microphysics parameterization for application in cloud and climate models, Part I: Description, *J. Atmos. Sci.*, *62*(2), 1665–1677.
Morrison, H., G. Thompson, and V. Tatarskii (2009), Impact of cloud microphysics on the development of trailing stratiform precipitation in a simulated squall line: Comparison of one- and two-moment schemes, *Mon. Weather Rev.*, *137*(3), 991–1007.
Muhlbauer, A., E. Berry, J. M. Comstock, and G. G. Mace (2014), Perturbed physics ensemble simulations of cirrus on the cloud system-resolving scale, *J. Geophys. Res. Atmos.*, *119*, 4709–4735, doi:10.1002/2013JD020709.
Murray, B. J., O'Sullivan, D., Atkinson, J. D., and Webb, M. E. (2012), Ice nucleation by particles immersed in supercooled cloud droplets, *Chem. Soc. Rev.*, *41*(19), 6519–6554.
Neale, R. B., et al. (2010), Description of the ncar community atmosphere model (CAM 5.0), NCAR/TN-486+STR, NCAR, Boulder, Colo. [Available at http://www.cesm.ucar.edu/models/cesm1.0/cam/docs/description/cam5_desc.pdf.]
Ovarlez, J., J. Gayet, and K. Gierens (2002), Water vapour measurements inside cirrus clouds in Northern and Southern hemispheres during INCA, *Geophys. Res. Lett.*, *29*(16), 1813, doi:10.1029/2001GL014440.
Penner, J. E., Y. Chen, M. Wang, and X. Liu (2009), Possible influence of anthropogenic aerosols on cirrus clouds and anthropogenic forcing. *Atmos. Chem. Phys.*, *9*(3), 879–896.
Phillips, V. T. J., DeMott, P. J., and C. Andronache (2008), An empirical parameterization of heterogeneous ice nucleation for multiple chemical species of aerosol, *J. Atmos. Sci.*, *65*, 2757–2783, doi:10.1175/2007JAS2546.1.
Pritchard, M., M. Moncrieff, and R. Somerville (2011), Orogenic propagating precipitation systems over the United States in a global climate model with embedded explicit convection, *J. Atmos. Sci.*, *68*(8), 1821–1840.
Pruppacher, H. R., J. D. Klett (1997), *Microphysics of Clouds and Precipitation*, 2nd ed., pp. 309–354, Kluwer Acad., Dordrecht, Netherlands.
Schmitt, C. G., and A. J. Heymsfield (2014), Observational quantification of the separation of simple and complex atmospheric ice particles, *Geophys. Res. Lett.*, *41*, 1301–1307, doi:10.1002/2013GL058781.
Shi, X., Liu, X., and Zhang, K. (2014), Effects of preexisting ice crystals on cirrus clouds and comparison between different ice nucleation parameterizations with the Community Atmosphere Model (CAM5), *Atmos. Chem. Phys. Discuss.*, *14*(12), 17,635–17,679.
Spichtinger, P., and K. M. Gierens (2009), Modelling of cirrus clouds–Part 1a: Model description and validation, *Atmos. Chem. Phys.*, *9*(2), 685–706.
Spichtinger, P., and M. Krämer (2004), Tropical tropopause ice clouds: A dynamic approach to the mystery of low crystal numbers, *Atmos. Chem. Phys.*, *13*(19), 9801–9818. doi:10.5194/acp-13-9801-2013.
Spichtinger, P., K. Gierens, and W. Read (2003), The global distribution of ice-supersaturated regions as seen by the Microwave Limb Sounder, *Q. J. R. Meteorol. Soc.*, *129*(595), 3391–3410. doi:10.1256/qj.02.141.
Spichtinger, P., K. Gierens, H. G. J. Smit, J. Ovarlez, and E. Polytechnique (2004), On the distribution of relative humidity in cirrus clouds, *Atmos. Chem. Phys.*, *4*, 639–647.
Tao, W. K., et al. (2009), A multiscale modeling system: Developments, applications, and critical issues, *Bull. Am. Meteorol. Soc.*, *90*(4), 515–534.
Tao, W.-K., J.-P. Chen, Z. Li, C. Wang, and C. Zhang (2012), Impact of aerosols on convective clouds and precipitation, *Rev. Geophys.*, *50*, RG2001, doi:10.1029/2011RG000369.
Waliser, D., et al. (2009), Cloud ice: A climate model challenge with signs and expectations of progress, *J. Geophys. Res.*, *114*, 1–27.
Wang, M., and J. E. Penner (2010), Cirrus clouds in a global climate model with a statistical cirrus cloud scheme, *Atmos. Chem. Phys.*, *10*(12), 5449–5474.
Wang, M., S. Ghan, M. Ovchinnikov, X. Liu, R. Easter, E. Kassianov, Y. Qian, and H. Morrison (2011a), Aerosol indirect effects in a multi-scale aerosol-climate model PNNL-MMF, *Atmos. Chem. Phys. Discuss.*, *11*, 3399–3459.
Wang, M., S. Ghan, R. Easter, M. Ovchinnikov, X. Liu, E. Kassianov, and Y. Qian (2011b), The multi-scale aerosol-climate model pnnl-mmf: Model description and evaluation, *Geosci. Model Dev.*, *4*, 137–168.
Wang, M., et al. (2012), Constraining cloud lifetime effects of aerosols using A-Train satellite observations, *Geophys. Res. Lett.*, *39*, L15709, doi:10.1029/2012GL052204.
Wang, Y., X. Liu, C. Hoose, and B. Wang (2014), Impact of heterogeneous ice nucleation by natural dust and soot based on a probability density function of contact angle model with the Community Atmospheric Model version 5, *Atmos. Chem. Phys. Discuss.*, *14*, 7141–7186, doi:10.5194/acpd-14-7141-2014.
Wielicki, B. A., B. R. Barkstrom, E. F. Harrison, R. B. Lee, G. L. Smith, and J. E. Cooper (1996), Clouds and the Earth's Radiant Energy System (CERES): An earth observing system experiment, *Bull. Am. Meteorol. Soc.*, *77*, 853–868.
Zhang, K., X. Liu, M. Wang, J. M. Comstock, D. L. Mitchell, S. Mishra, and G. G. Mace (2013), Evaluating and constraining ice cloud parameterizations in CAM5 using aircraft measurements from the SPARTICUS campaign, *Atmos. Chem. Phys.*, *13*(9), 4963–4982, doi:10.5194/acp-13-4963-2013.
Zhang, Y., et al. (2008), On the diurnal cycle of deep convection, high-level cloud, and upper troposphere water vapor in the Multiscale Modeling Framework, *J. Geophys. Res.*, *113*, D16105, doi:10.1029/2008JD009905.